Article

Controlled Size Growth of Thermally Stable Organometallic Halide Perovskite Microrods: Synergistic Effect of Dual-Doping, Lattice Strain Engineering, Antisolvent Crystallization, and Band Gap Tuning Properties

Mohammed Nazim and Jae Hyun Kim*

Read Online

ACCESS | Metrics & More | Article Recommendations | Supporting Information

ABSTRACT: Organometallic halide perovskites, as the light-harvesting material, have been extensively used for cost-effective energy production in high-performance perovskite solar cells, despite their poor stability in the ambient atmosphere. In this work, methylammonium lead iodide, $CH_3NH_3PbI_3$, perovskite was successfully doped with $KMnO_4$ using antisolvent crystallization to develop micrometer-length perovskite microrods. Thus, the obtained $KMnO_4$-doped perovskite microrods have exhibited sharp, narrow, and red-shifted photoluminescence band, as well as high lattice strain with improved thermal stability compared to undoped CH_3NH_3PbI. During the synthesis of the $KMnO_4$-doped perovskite microrods, a low boiling point solvent, anhydrous chloroform, was employed as an antisolvent to facilitate the emergence of controlled-size perovskite microrods. The as-synthesized $KMnO_4$-doped perovskite microrods retained the pristine perovskite crystalline phases and lowered energy band gap ($\sim$1.57 eV) because of improved light absorption and narrow fluorescence emission bands (fwhm < 10 nm) with improved lattice strain ($\sim$4.42 $\times$ 10^{-5}), Goldsmith tolerance factor ($\sim$0.89), and high dislocation density ($\sim$5.82 $\times$ 10^{-4}), as estimated by Williamson−Hall plots. Thus, the obtained results might enhance the optical properties with reduced energy band gap and high thermal stability of doped-perovskite nanomaterials in ambient air for diverse optoelectronic applications. This study paves the way for new insights into chemical doping and interaction possibilities in methylamine-based perovskite materials with various metal dopants for further applications.
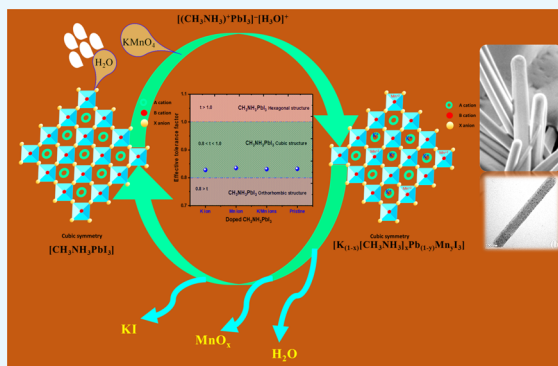
INTRODUCTION

Organometallic halide perovskite (OMHPVs and MAPbX$_3$) materials have been extensively applied as light-harvesting materials for various applications, despite low stability in moisture, heat, and light.[1−3] The crystal structure of perovskite materials provides distinct information of phase purity, bond length and bond angles, and inter- or intramolecular interactions to tune electrical and optical properties.[4] Owing to the various striking features including long lifetime, high absorption wavelength spectra with a small-energy band gap, and large charge-carrier diffusion length, OMHPVs have gained enormous buzz in search of the promising and cheaper alternatives for renewable energy applications.[5,6] The solution-based chemical-doping process induces defects in the crystal lattice of the OMHPVs, which contribute to boost the charge-transfer properties, tuning of the energy band gap, and stabilize the crystal structure via strain engineering and phase transformation as a function of temperature.[7,8] The optical band gap derives the emission properties of the doped and undoped perovskite materials via the state-of-the-art optoelec-

tronic devices.[9,10] The structure of perovskite materials can be represented using the general formula ABX$_3$, in which various A$^+$ cations, such as methylammonium (CH$_3$NH$_3^+$ and MA$^+$) cations, occupy the central position of the corner-shared (PbI$_6$)$^{4-}$ octahedrons of perovskite.[11] To modulate the crystal lattice structure of OMHPVs, various solution-doping strategies might partially or completely replace the divalent metal cations of (ABX$_3$) as A, B, and X and consequently offer a large number of chemical-doping possibilities.[12,13] In particular, in the crystal structure of methylammonium lead iodide hybrid perovskite consisting of a corner-sharing BX$_6$ octahedral, B is a divalent metal cation, A is a monovalent organic cation which occupies voids existing between the
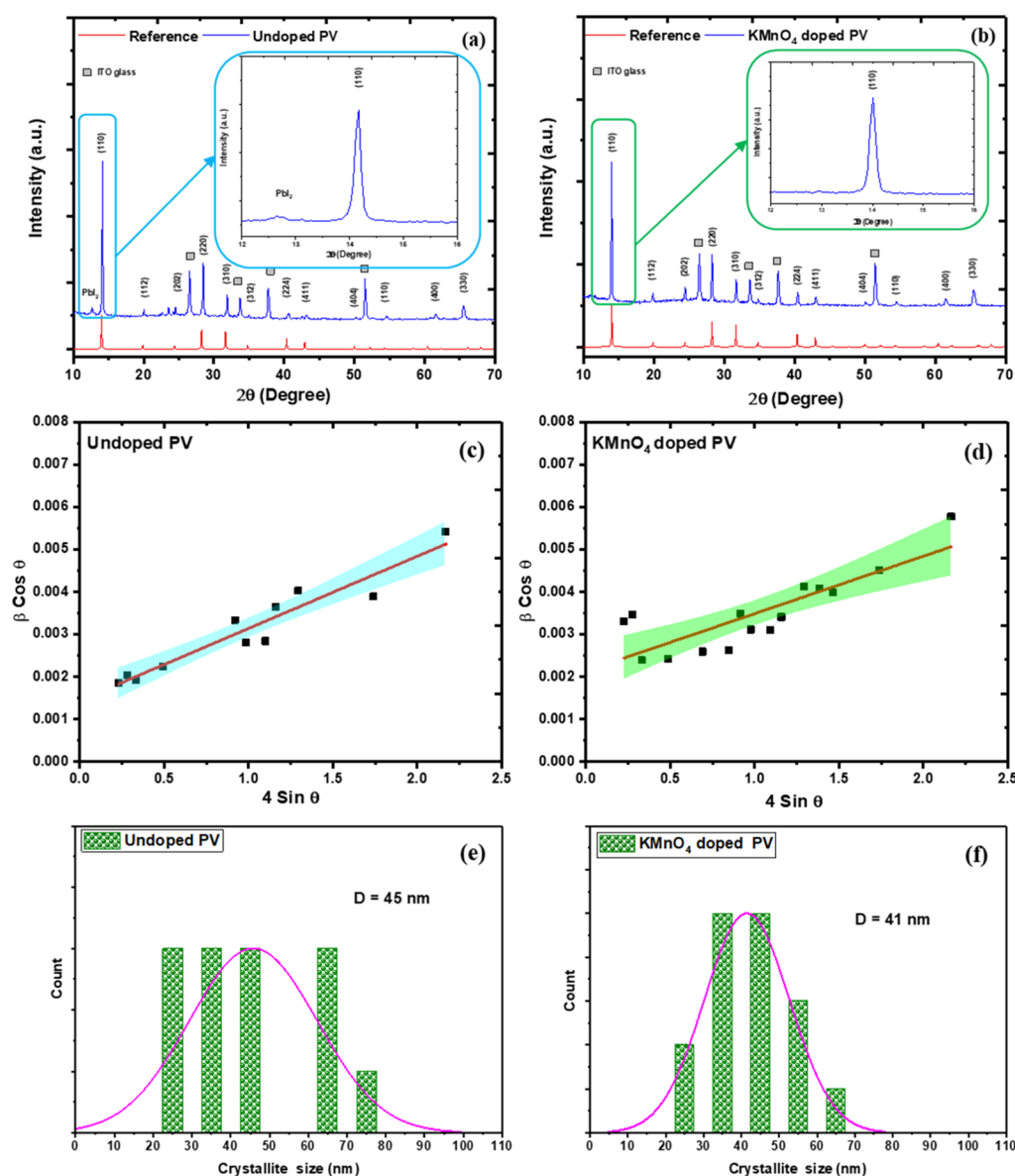
Figure 1. XRD spectra of (a) undoped PV (b) KMnO$_4$-doped PV with inset high-intensity typical perovskite peak and W—H plots of the of (c) undoped PV (d) KMnO$_4$-doped PV, histogram profile of the crystallite size (e) undoped PV (f) KMnO$_4$-doped PV.

adjacent octahedral, and X is a halide such as I, Br, or Cl.[14] In hybrid perovskites, the shape, size, orientation, and charge distribution of all the three A, B, and X components play a crucial role in tuning the optical and physical properties for high stability of the perovskite structure.[15,16] Subsequently, the existence of a dimethylformamide (DMF)-induced intermediate phase was observed via X-ray diffraction (XRD) during perovskite crystallization. Additionally, the interplanar distances of the DMF-intermediate phase support homogeneous nucleation for the perovskite crystal growth.[17,18]

In particular, the partial or complete substitution of any components induces lattice distortions during perovskite crystallization, which eventually suppresses the rate of crystal growth.[19] Furthermore, chemical doping might increase the charge diffusion length in the active layer and behave like an additive which leads to homogeneous and crystalline perovskite films.[20] For undoped and doped OMHPV materials, a cost-effective and simple approach, antisolvent crystallization has been applied to tackle crystal-growth rate, nucleation, and

crystal morphologies.[21] In methylammonium-based perovskites, various anhydrous solvents have been applied for antisolvent crystallization as toluene, chlorobenzene, chloroform, acetone, methanol, and so forth to address the challenges of the perovskite morphology using a cost-effective solvent treatment approach to grow highly oriented crystallites with controlled grain sizes and low pinhole densities.[22] Manganese is one of the most abundant metals with low toxicity in the Earth's crust which is considered as the prime candidate to replace of toxic lead metals of the halide perovskite materials.[23] The chemical doping of the Mn^{2+} cation is intended to partial substitution of the Pb^{2+} cation and reduces toxicity to tune optical and electric properties in the doped perovskite materials.[24] The transition-metal Mn^{2+} ion-doped perovskite nanocrystals suppress the formation of high-density defects and trap states as nonradiative centers with partial interstitial doping of MA cations.[25] However, the doping concentration of the dopant significantly derives the performance of the perovskite materials. Recently, Klug et al. demonstrated the

Table 1. Structural Parameters of Perovskite Microrods Obtained from XRD Spectral Plots

OMHPVs	crystallite size (nm)	fwhm (nm)	crystallinity (%)	tolerance factor (t)	dislocation density $\times 10^{-4}$ (nm^{-2})	strain $\times 10^{-5}$ (ε)
undoped PV	45	0.21	87	0.832	4.77	2.88
$KMnO_4$ doped PV	41	0.22	83	0.831	5.82	4.42

partial substitution of Pb^{2+} cations by transition- or alkaline-earth metals.[26] In addition, transition metal-doped lead halide perovskite nanocrystals and nanoplatelets have been reported by partial replacement of Pb^{2+} with Mn^{2+} cations.[27,28] As potassium cations (K^+ cations) are also abundant metals in the Earth's crust, and they are also cost effective and have low toxicity to be promising candidates for doping in halide perovskite materials.[29] The chemical doping of alkali metals (Na^+ and K^+ ions) greatly influences the film morphology and crystallinity of $MAPbI_3$ materials and smaller ionic size of alkali metals facilitates them to occupy the interstitial position in the perovskite crystal lattice.[30] Indeed, potassium doping might improve the crystallinity, enhance stability, and leads to longer carrier lifetimes by the insertion in to the interstitial sites and partially replace MA cations.[31,32]

In this work, $KMnO_4$ was employed as a dopant to produce simultaneous metal cations doping in the OMHPVs. The results clearly proved the insertion of potassium and manganese cations into the perovskite lattice structure and partial replacement of the Pb^{2+} cations. Through XRD patterns, X-ray photoelectron spectroscopy (XPS), and time-of-flight secondary-ion mass spectrometry (TOF-SIMS) analysis, it was determined that the simultaneous incorporation of metal cations significantly boosted the optical (Tauc plots and Urbach plots) and enhanced thermal stability of the $KMnO_4$-doped perovskite microrods. Specifically, $KMnO_4$ doping in perovskite might significantly reduce the grain boundaries and crystal defects and suppress nonradiative recombination losses. Using the Williamson–Hall (W–H) analysis, various parameters were calculated as crystal lattice strain, dislocation density, Goldsmith tolerance factor, and so forth for the undoped and $KMnO_4$-doped perovskite microrods which facilitates the unique feature of $KMnO_4$-doped perovskite microrods for further applications.

■ RESULTS AND DISCUSSION

XRD Analysis and Degree of Crystallinity. To determine the lattice structure and various phase conversion of perovskites, the XRD patterns (Figure 1a,b) of the undoped and $KMnO_4$-doped perovskite were measured at room temperature. In XRD spectra, the undoped or pristine organometallic hybrid, $CH_3NH_3PbI_3$ perovskite, showed highly crystalline diffraction peaks of (110) and (220) crystal phases at 14.14 and 28.46° which slightly lowered the peak angles to 14.01 and 28.24°, respectively, after doping with $KMnO_4$. The peak index of undoped and doped perovskite microrods (Figure 1a,b) displays a total absence of a tetragonal phase characteristic peak at 23.5° for pristine $CH_3NH_3PbI_3$ compared to the reference (ICSD no. 250735) $CH_3NH_3PbI_3$ perovskite with a cubic-phase symmetry.[33,34] During solution-doping, undoped and doped perovskite microrods displayed low-intensity intermediate-phase transformation of the solvent interaction after annealing, resulting in slow and continuous crystallization of perovskites. Because of the intercalation of the DMF solvent in the $CH_3NH_3PbI_3$ perovskite, three low intensity peaks were found near <10° (2θ = 6.53, 8.01, 9.56°) which might be due to the Lewis adduct, $MAPbI_3 \cdot DMF$

complex formation, and led to a slight enlargement of the perovskite lattice structure. With the undoped perovskite, the low-intensity diffraction peak at ~12.6° was attributed to unconverted PbI_2 crystals (Figure S1a), suggesting the high coordination tendency of the DMF solvent with $MAPbI_3$. The comparative XRD spectra of pristine PbI_2 with undoped and $KMnO_4$-doped perovskite films exhibit the full conversion of perovskite and slight lowering of the peak intensity after $KMnO_4$ doping. The Lewis adduct and excess PbI_2 peaks displayed a lower intensity after $KMnO_4$ doping, which created deformation and defects in the perovskite lattice structure.[35] Furthermore, annealing of the doped perovskite at high temperature leads to an enhanced lattice vibration with reduced crystallinity and shifts the perovskite peaks toward lower diffraction angles. However, the strongest (110) peak ~14.01° of the $KMnO_4$-doped $CH_3NH_3PbI_3$ (Figure 1b) perovskite showed a slightly lower intensity with an increasing full width half maximum (fwhm) of 0.14 nm (Figure S1b), compared to 0.13 nm of the undoped $CH_3NH_3PbI_3$ perovskite.[36] The overall change in the fwhm values as a histogram profile (Figure S1c,d) was presented for various XRD peaks.

To synthesize doped perovskite microrods, it is critical to control the nucleation of crystal growth of perovskite and prevent aggregation which induces physical and chemical properties.[37] Theoretically, the insertion of K^+ cations into the perovskite crystal structure is an energetic phenomenon at interstitial positions, which gradually lowers the Frenkel-defect sites, with no induction of K^+ cations into the A-site of the perovskite crystal lattice. Doping with $KMnO_4$ provides a kind of double doping of alkali metal cation, K^+, and the transition-metal cation, Mn^{2+}, in the perovskite crystal lattice simultaneously. K^+ cation doping might improve the grain size and crystallinity by reducing the crystallization activation energy, resulting in fewer crystal defects and improved film morphology. On the other hand, the transition-metal cation, Mn^{2+}, might influence the pristine methylammonium lead halide perovskite crystal structure, leading to a dramatic phase change toward the cubic phase at room temperature.[38] The broadening of peaks indicates grain refinement with the large strain properties of the powder materials. The average crystal grain size was calculated for the undoped and $KMnO_4$-doped perovskites using the Debye−Scherrer formula

$$D = \frac{K\lambda}{\beta \cos \theta} \tag{1}$$

where D = crystallite size, β = line broadening at fwhm values, K = shape factor (0.94), λ = X-ray wavelength of the Cu Kα radiation, and θ is the Bragg angle.

The grain boundaries and large pinholes densities suppress the perovskite device performances because of a large number of trap-assisted recombination centers and lower carrier mobilities.[39] The crystallite size (Figure 1c,d) of undoped perovskite display slight reduction from ~45 to ~41 nm after $KMnO_4$ doping at room temperature. The histogram profile of the crystallite size (Figure 1e,f) was also displayed for undoped and $KMnO_4$-doped perovskite. Additionally, perovskite films with low pinholes drive the reduced recombination points,

which facilitates ultrafast electron-transportation.[40] To identify large grain sizes, various solvents as toluene, chlorobenzene, and so forth have been applied to produce uniform thin perovskite films with minimized pinholes. Additionally, the degree of crystallinity (Table 1) indicates the positions of various atom or molecular arrangements in powder materials. It can be calculated using the following relation

$$\text{crystallinity (\%)}$$
$$= \frac{\text{total area of crystalline peaks}}{\text{total area of all (crystalline and amorphous) peaks}}$$
$$\times 100 \tag{2}$$

Furthermore, the degree of crystallinity of microrods slightly decreases from ~87 to ~83% after doping of $KMnO_4$ compared to the undoped perovskite microrods, revealing the reduced crystalline nature of microrods.

W−H Analysis and Strain Engineering. The W−H analysis is a simplified integral method where both size-induced and strain-induced broadening are deconvoluted and used to estimate the crystallite size and lattice strain of organometallic hybrid perovskite materials. The W−H plot (Figure 1c,d) of the undoped and $KMnO_4$-doped perovskites showed the differences in lattice strain before and after $KMnO_4$ doping of the perovskites because of crystal imperfections and various dislocation densities near the grain boundaries. The lattice strain (ε) induced in powders because of crystal imperfection and distortion was calculated using the formula

$$\varepsilon = \frac{\beta}{4 \tan \theta} \tag{3}$$

as the crystallite size and strain contribute to structural line broadening of XRD peaks. The low d-spacing XRD peaks exhibit large peak broadening of the crystalline materials in the ordered structure.

$$\beta = \frac{K\lambda}{D \cos \theta} + 4\varepsilon \tan \theta \tag{4}$$

The $KMnO_4$-doped $CH_3NH_3PbI_3$ exhibits a slightly decreased grain size (Table 1) with an enhanced crystal-lattice distance (d spacing) of 2.2 Å as compared to undoped perovskite of the crystal-lattice distance of 2.1 Å for the full XRD spectrum. Furthermore, the calculated lattice strain of the $KMnO_4$ doped perovskite was determined to be ~4.42×10^{-5} compared to the lattice strain (~2.89×10^{-5}) of the undoped perovskites that reveals the insertion of $KMnO_4$ in perovskite to stabilize the crystal lattice by reducing the phase conversion at room temperature. The strain of pure perovskite increases with doping of $KMnO_4$ which indicates the modified atomic arrangement, and the phase purity of the $KMnO_4$-doped perovskite microrods.

The dislocation density (δ) of the doped perovskite material provides the total length of the dislocation lines per unit volume of the crystal lattice. The δ value of the undoped and $KMnO_4$-doped perovskite materials was obtained using the Williamson and Smallman relation as

$$D^2 \cdot \delta = 1 \tag{5}$$

Thus, the dislocation density of the $KMnO_4$-doped perovskite was significantly improved ($\delta = 5.82 \times 10^{-4}$) after doping with $KMnO_4$ compared to the undoped perovskite ($\delta = 4.77 \times 10^{-4}$) crystal lattice.

Owing to phase transformation, the atomic positions change in the crystal lattice of the doped $MAPbI_3$ and cubic octahedral crystal structure. Because of $KMnO_4$ doping, it might be assumed that the alkali ion, K^+ ion (ionic radius = 138 pm), partially replaces the MA^+ cation (ionic radius = 180 pm) due to its smaller radius. Additionally, the transition-metal ion, Mn^{2+} (ionic radius = 83 pm), has shown the ability to partially replace the Pb^{2+} ion (ionic radius = 120 pm) to form a doped perovskite simultaneously. Goldschmidt's tolerance factor (t) was employed to perfectly predict the doping defects and crystal deformation of various perovskite structural stabilities using ionic-radius. Goldschmidt's tolerance factor was calculated using the following equation

$$t = \frac{(R_A + R_X)}{\sqrt{2}(R_B + R_X)} \tag{6}$$

where R_A, R_B, and R_X are the ionic radii of A = $[CH_3NH_3^+]$ cation, B = Pb^{2+} or Mn^{2+} cation, and X = I^- anion, respectively. When Goldschmidt's tolerance factor follows the range $0.8 < t < 1$, the material can be expected to have a cubic structural geometry. As divalent Mn^{2+} ions might efficiently adjust in place of the Pb^{2+} ion of perovskite because of the small $Mn-I$ bond length of 2.9 Å compared to the $Pb-I$ bond length of 3.20 Å which leads to high stability for $KMnO_4$-doped perovskite.[41] Hence, $KMnO_4$-doped perovskite microrods might be proposed as the $K_x(CH_3NH_3)_{1-x}Mn_yPb_{1-y}I_3$ structure which produce the effective t value (Table 1) of ~0.831 with the retention of the original structural geometry of perovskite.[32] After doping with $KMnO_4$, effective ionic radii $(R_{effective})$ of the both A and B cations were modified because of the partial substitution of the MA^+ and Pb^{2+} cations by K^+ and Mn^{2+} cations, respectively. The effective radii of the $KMnO_4$-doped perovskite $K_{0.054}(CH_3NH_3)_{0.946}Mn_{0.042}Pb_{0.958}I_3$ microrods might be accurately calculated using the relations as $R_{A(effective)} = xR_{A'} + (1-x)R_{A''}$ and $R_{B(effective)} = yR_{B'} + (1-y)R_{B''}$ where $R_{A(effective)}$ and $R_{B(effective)}$ are the effective ionic radius of the doped perovskite, x and y are the doping percentage of the K^+ ion and Mn^{2+} ions, respectively, $R_{A'}$ is the ionic radius of the R_{K^+} cation, $R_{A''}$ is the ionic radius of R_{MA^+}, $R_{B'}$ is the ionic radius of the $R_{Mn^{2+}}$ cation, $R_{B''}$ is the ionic radius of the Pb^{2+} cation. Furthermore, the effective Goldsmith tolerance factor of the $KMnO_4$-doped perovskite microrods can be precisely estimated using the modified formula of the eq 6 as: $t = \frac{(R_{A(effective)} + R_X)}{\sqrt{2}(R_{B(effective)} + R_X)}$. Hence, the effective Goldsmith tolerance factor of doped perovskite also follows the stability range $0.8 < t < 1$ corresponding to the cubic perovskite structure which displays the efficient metal doping without disturbing the original structure of perovskite.[42] The effective doping and replacement of metal cations of perovskite might be due to the smaller ionic radius of the K^+ ion and Mn^{2+} ions compared to the MA cation and Pb^{2+} cations, respectively, and it produces high thermal and structural stability to the metal-doped perovskite microrods.[43] Meanwhile, the bond length of B−X also has a significant impact on the energy band gap, with the latter decreasing as the former increases, resulting in an extension of the absorption spectrum. Owing to toxic nature, the use of Pb can have adverse effects on the environment, and life safety development has hindered the commercialization of PSCs.[44]

Ultra-High Resolution Field-Effect Scanning Electron Microscopy/Elemental Mapping. The morphology and
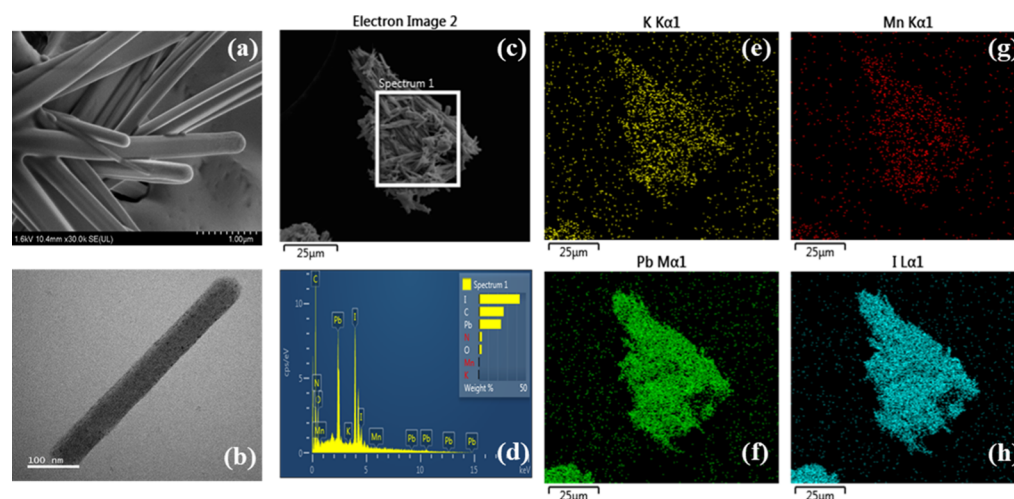
Figure 2. KMnO$_4$-doped perovskite microrods (a) UHR-FESEM image (b) TEM image of a single microrod (c) UHR-FESEM image of KMnO$_4$-doped perovskite microrods, (d) EDX analysis of the selected part, UHR-FESEM elemental mapping image of (e) potassium element (f) lead element (g) manganese element, and (h) iodine element.

microstructures of undoped and KMnO$_4$-doped perovskite powder were examined by using the ultra-high resolution field emission scanning electron microscopic (UHR-FESEM) images. The obtained undoped perovskite microrods (Figure 2a) possess a length of less than <10 μm and a width of less than <2 μm. Additionally, charge migration might enable the alkali-doped perovskite materials with interfacial ions to efficiently promote charge transport. The strong oxidizing agent, KMnO$_4$, was employed as the dopant for the CH$_3$NH$_3$PbI$_3$ microrods because of the positive redox potential of MnO$_4^-$/Mn^{2+} (NHE, 1.51 V). Interestingly, the KMnO$_4$-doped perovskite microrods showed an enhanced length but slight decrease in width after dual-doping and annealing at 100 °C for 10 min.[45] In the high-resolution transmission electron microscopy (HR-TEM) images (Figure 2b), the excellent lattice spacing and sharp pattern line with well-defined spots reveals the crystalline nature of the KMnO$_4$-doped CH$_3$NH$_3$PbI$_3$ microrods. The KMnO$_4$-doped microrods suggest well-matched surface stoichiometry with an interplanar distance (d) of ∼2.8 Å which is slightly higher than the results obtained in the XRD patterns (∼2.2 Å) of d-spacing of the crystal lattice.[45] Furthermore, the identical d-spacing indicates similar crystallite grain orientation and crystallinity leads to retained the cubic phase structure for KMnO$_4$-doped microrods. Interestingly, the K$^+$ cation doping managed to suppress halide migration as well as lower band gap energy.[46] Additionally, the doped K$^+$ cation might have attracted excess halides at the grain boundaries to form potassium iodide and create vacancies which eventually reduced halide migration.[47] UHR-FESEM elemental mapping images (Figure 2e−g) of KMnO$_4$-doped perovskite microrods showed efficient and uniform distribution of K, Pb, Mn, and I elements with maintaining the overall Pb/I ratio of 1/3.03 (Figure 2d) which reveals the insertion of metal ions in the perovskite crystal lattice, even at the edges of the microrods. Owing to its small size, the K$^+$ ion might be inserted into the interstitial positions in the perovskite crystal lattice, resulting in larger lattice interplanar spacing. The K$^+$ ion has a small ionic radius (r = 0.138 nm) compared to the methylammonium, CH$_3$NH$_3^+$ (r = 0.120 nm) cation. The migration of ions was significantly hampered in the perovskite lattice because

interstitial positions were occupied with alkali cations, resulting in the hysteresis behavior. With the introduction of alkali cations (K$^+$) into the methylamine-perovskite materials via solution-based chemical doping, the small-sized alkali cations preferably occupied the interstitial positions, as compared to the A cation substitution with lattice expansion.[48]

Energy-Dispersive X-ray Spectroscopy Analysis. Energy-dispersive X-ray (EDX) spectroscopy (S2) analyzes to probe the exact weight percentage or elemental ratio of various elements. For undoped perovskite microrods, EDX spectroscopy analysis indicated the I/Pb atomic ratio of ∼2.87 ± 0.02 along with the images (Figure S2a,c) which well follows the PbI$_3$ stoichiometry of the pristine perovskite. In the KMnO$_4$-doped perovskite, microrods lead to the I/Pb atomic ratio (Figure S2b,d) of 3.03 ± 0.02 which matched well with elemental stoichiometry and attributed to the excess halides that were engaged with K$^+$ cations or Mn^{2+} ions and the additional amount of dopant at the interstitial positions. In addition, the optimized doping concentration of doped cations can be estimated as the doping percentage of ∼5.39 and ∼4.18% for K$^+$ ion and Mn^{2+} ions in place of MA$^+$ and Pb^{2+} ions, respectively, for KMnO$_4$-doped perovskite microrods. Additionally, the occupation of interstitial positions with alkali ions seems to increase the ion-migration barriers in the perovskite crystal-lattice structure, by interaction with halides.[49]

UV−Visible Spectra, Tauc Plots, and Band Gap Engineering. The absorption spectra of pristine PbI$_2$, undoped CH$_3$NH$_3$PbI$_3$, and KMnO$_4$-doped CH$_3$NH$_3$PbI$_3$ perovskite in thin films on indium tin oxide (ITO) substrates (Figure 3a) revealed the optical properties of the materials. For perovskite materials, the Tauc plots (Figure 2c) were applied for band gap estimation through the absorption spectrum as the difference of valence bands (VBs) and conduction bands (CBs).[50] The corresponding energy band gap (E_g) was determined with extrapolation of the linear region of the Tauc plots toward x-axis using the following equations
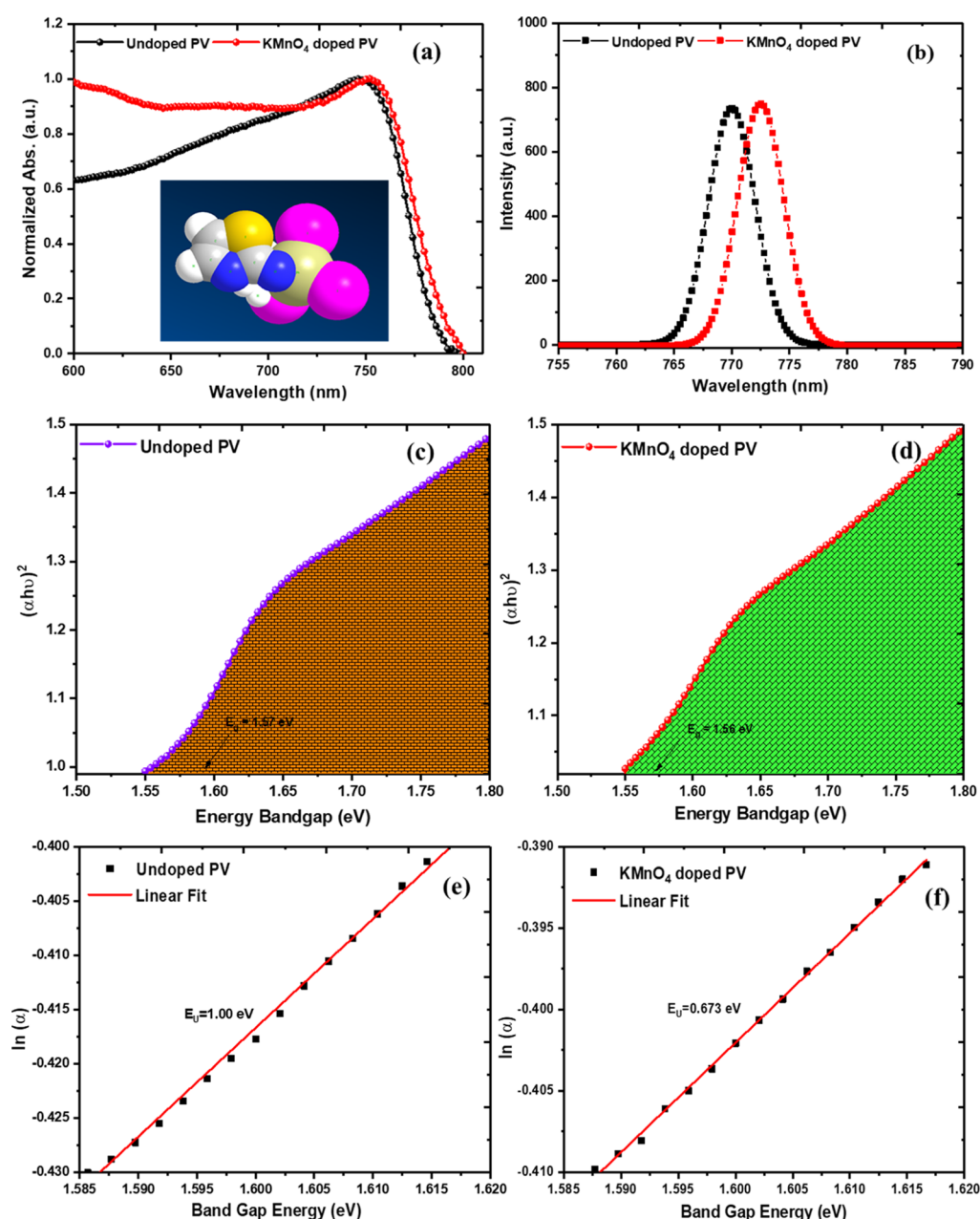
$$\alpha h\nu = A(h\nu - E_g)^2 \tag{7}$$

Figure 3. (a) Absorption spectra of undoped and KMnO$_4$-doped PV with the inset perovskite model (b) fluorescence peaks of undoped and KMnO$_4$-doped PV and Tauc plot of (c) undoped PV (d) KMnO$_4$-doped PV applied for energy band gap calculation, Urbach plots for (e) undoped PV and (f) KMnO$_4$-doped PV.

where α is the absorption coefficient, $h\nu$ is the photon energy, A is a constant, and E_g is the energy band gap which can be calculated using the following equation

$$E_g = 1240/\lambda_{edge} \qquad (8)$$

where λ_{edge} can be found from the UV−visible absorption spectra. Furthermore, the energy band gap decreases with increased crystal ordering of the perovskite materials. In addition, the strong relaxation and re-orientation of the organic cations (methyl amine cation, MA) result in pseudo-cubic or tetragonal-like structure for the perovskites.[51]

The absorption onset of the yellow-colored PbI$_2$ films occurred around a wavelength of ∼545 nm with a high energy band gap of ∼2.28 eV obtained from the Tauc plot (Figure S3a,b) at room temperature. In continuation, the complete

conversion of PbI$_2$ into CH$_3$NH$_3$PbI$_3$ was assessed by the change of the yellow color (PbI$_2$) film to the dark brown color film of perovskites with the enhancement of absorption wavelength onset and low-energy band gap after annealing at 100 °C for 10 min. From the absorption spectrum (Figure 3), the absorption onset value of undoped CH$_3$NH$_3$PbI$_3$ films estimated as ∼786 nm (Table 2) corresponds to an energy band gap of ∼1.57 eV as obtained from the Tauc plot (Figure 3c), indicating the formation of undoped CH$_3$NH$_3$PbI$_3$. Additionally, KMnO$_4$-doped perovskite thin films also displayed a high wavelength absorption onset value of ∼792 nm and explore a low energy band gap of ∼1.56 eV, as estimated from the Tauc plot (Figure 3d) compared to the undoped CH$_3$NH$_3$PbI$_3$. On increasing electronegativity of the M and X ions, the energy band gap generally increases for

Table 2. Optical Parameters of the Perovskites Extracted from UV−Visible and PL Spectral Analysis

OMHPVs	abs. edge[a] (λ_{edge}) (nm)	PL[b] λ_{max} (nm)	energy band gap[c] (eV)	Urbach energy[d] (E_U) (eV)	PL_{fwhm}[e] (nm)
undoped PV	786	770	1.57	1.00	5.64
$KMnO_4$ doped PV	792	772	1.56	0.67	5.17

[a]Estimated from the absorption spectra of PV films. [b]Maximum intensity fluorescence peak of PV films. [c]Obtained from the Tauc plots. [d]Estimated from the $\ln(\alpha)$ vs energy band gap plots. [e]Calculated from the Gaussian fit curve of fluorescence spectral peaks.

semiconductors. The metal-ion doping results either in alloys with the host metal because of partial replacement or insertion of transition metal ions in the perovskite crystal lattice Furthermore, the insertion of transition-metal ions into the perovskite lattice influences the charge-transfer between the dopant metal ions and methylamine-based perovskite crystals.[52]

Photoluminescence Spectra of Doped Perovskite Films. Using one-step deposition, the photoluminescence (PL) spectra (Figure 3b) of the undoped $CH_3NH_3PbI_3$ films showed a sharp and symmetric emission band centered around ∼770 nm with the excitation wavelength of 500 nm, corresponding to 12,987.01 cm^{-1}, which matches the absorption-onset criteria of pristine $CH_3NH_3PbI_3$ films. For undoped perovskite, the high-energy emission band displayed a narrow fwhm value of 5.64 nm (Figure S3c) with a Gaussian fit curve (at r^2 = 0.99807) because of strong intramolecular

charge-transfer interactions and the edge effect of the nanomaterials.

Variable sizes of nanomaterials directly affect the wavelength of fluorescence emission bands, resulting in tunable energy band gaps. Furthermore, the $KMnO_4$-doped perovskite exhibited a symmetric, low-energy fluorescence band at ∼772 nm corresponding to 12,953.37 cm^{-1}, suggesting the doping of $KMnO_4$ into the methyl ammonium lead iodide perovskite lattice without any change in its original lattice structure.[53] Interestingly, the fluorescence spectra of the $KMnO_4$-doped perovskite exhibited a red-shifted fluorescence band with high intensity and a reduced fwhm of 5.17 nm (Figure S3d) with a Gaussian fit curve (at r^2 = 0.99870) compared to undoped perovskite at room temperature. The narrow bandwidth (less than <10 nm) of the PL spectral peaks reveals the homogenous growth of the $KMnO_4$-doped perovskite microrods. The insertion of the potassium cation proved to be beneficial for charge-carrier transportation and shrank the PbI_6 octahedron volume, increasing the bond strength and phase stability. Additionally, the simultaneous doping of the transition-metal cation, Mn^{2+}, might fulfill the trap-density crystal phase but decreased the grain size by partial replacement of the Pb^{2+} cations. Owing to a large difference in ionic radius ($R_{Mn(II)}$ = 83 pm high spin and $R_{Pb(II)}$ = 120 pm), the incorporation of the Mn^{2+} cation might create more defects in the crystal lattice, along with the alkali-metal, K^+, interaction with halide anions. After doping with $KMnO_4$, the rigid crystal structure of the perovskite acquired slight deformational changes and created minor defects at interstitial positions, owing to the small Stokes shift and low band gap energy.[54]

Urbach Energy (E_U) Estimation. In optical absorption spectra, an electron of the VB gets excited into the CB and its
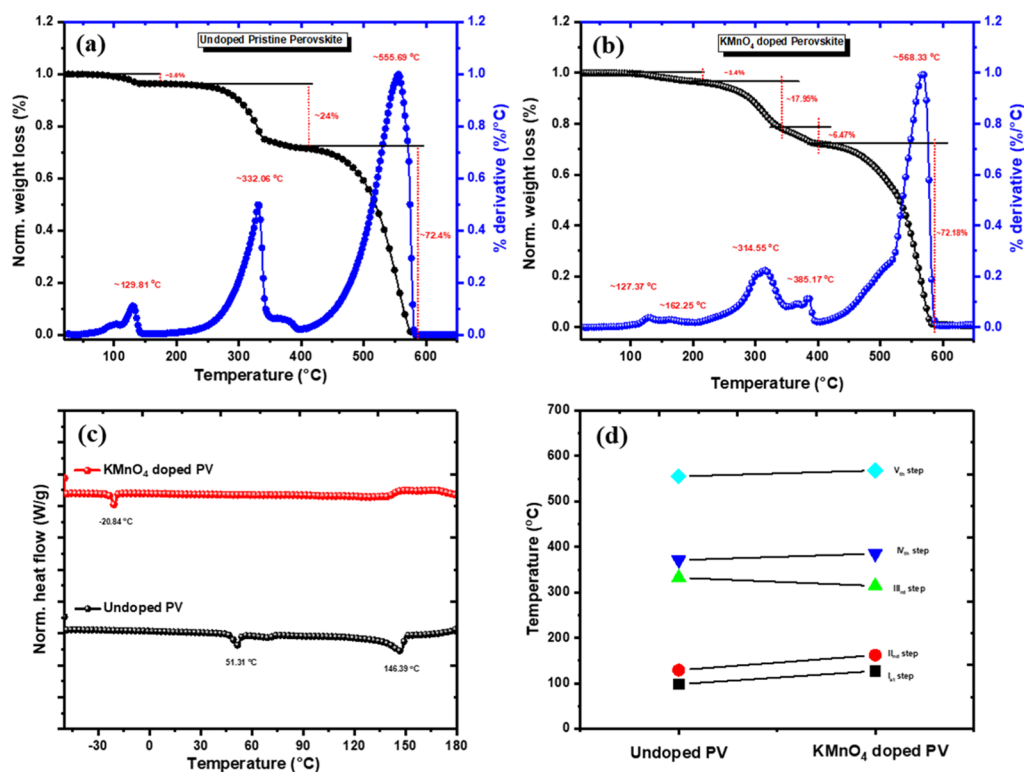

Figure 4. Thermogravimetric plots (black line) of (a) undoped perovskite with weight-loss steps, (b) $KMnO_4$ doped perovskite with their corresponding percentage-derivative curves (blue line) in the nitrogen atmosphere, (c) DSC curves of undoped (black line) and $KMnO_4$-doped perovskite (red line) microrods, and (d) comparison of TGA degradation steps of undoped and $KMnO_4$-doped perovskite microrods.
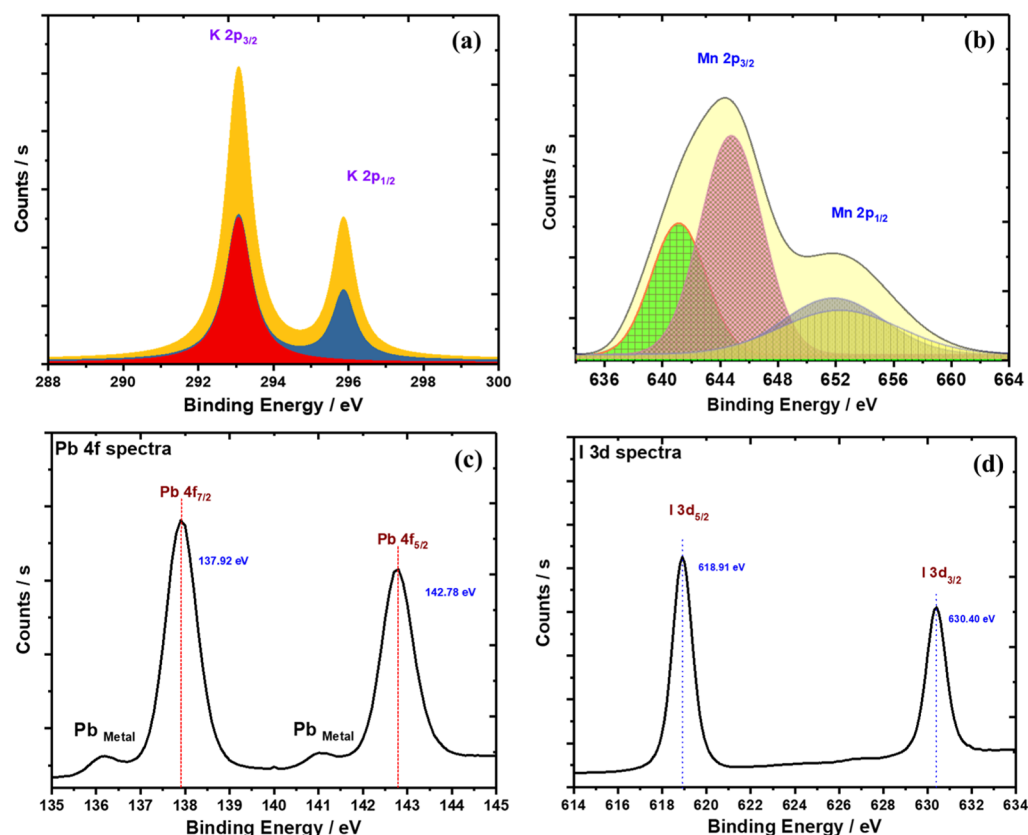
Figure 5. XPS spectral plots various elements (a) K 2p spectrum, (b) Mn 2p spectrum, (c) Pb 4f spectrum, and (d) I 3d spectrum of KMnO$_4$-doped perovskite.

difference is considered as the energy band gap. On light irradiation, the doped materials trap the excited electrons in the defect states to prevent direct transition to the CB. The defect states of the materials are accountable for the absorption tail which is called as Urbach tail.[55] Consequently, the energy associated with this tail is referred to as Urbach energy (E_U) which is exponentially dependent on the absorption coefficient (α). In nanomaterials, Urbach energy (Figure 3e,f) is the crucial parameter related to the crystallinity and the disorder of crystal structures. In the low photon-energy range, the Urbach empirical rule is given using the following equation
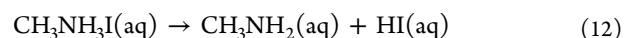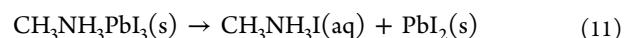
$$\alpha = \alpha_o \exp(h\nu/E_U) \tag{9}$$

where α_o is a constant and E_U denotes the energy of the band tail or Urbach energy. E_U is weakly dependent on temperature and related to the localized states of disordered or low crystalline materials. Taking the logarithm of the above-mentioned equation

$$\ln \alpha = \ln \alpha_o + (h\nu/E_U) \tag{10}$$

The Urbach energy of the KMnO$_4$-doped perovskite exhibits a lower value (E_U = 0.67 eV) compared to the undoped perovskite (E_U = 1.00 eV), which indicates eternal random shuffling motion of atoms in the stacked structure of the amorphous material. Hence, reduced vibrational energy levels diminish the multiplicity in transitions, resulting in lower E_U.[56]

Thermal Analysis of Perovskite Micro-rods. Thermogravimetric analysis (TGA) is used to determine the mass loss profile of the organic and inorganic components of organometallic perovskite, CH$_3$NH$_3$PbI$_3$ microrods as a function of temperature. The thermal behavior of the organic component

is used to interpret the TGA data of various perovskite precursors as well as CH$_3$NH$_3$PbI$_3$ microrods. The TGA data (Figure 4) of the undoped MAPbI$_3$ and KMnO$_4$-doped MAPbI$_3$ powder (DMF solvent) are presented to better compare the structural properties of perovskite before and after doping. The fraction of weight loss (~3%) starting at around ~110 °C might be assigned to the dehydration reaction of the remaining solvent and humidity in the perovskite. Furthermore, the two small mass losses take place at ~85 and ~125 °C, clearly visible as two small minima in the first derivative (Figure 4a) because of the removal of absorbed H$_2$O from the perovskite material. Additionally, the weight loss (~23.8%) in the temperature range around ~250−320 °C belongs to the loss of methylammonium iodide (MAI), and the temperature range of ~440−580 °C could be assigned to the decomposition of PbI$_2$ (weight loss of ~71.3%) crystals. The perovskite microrods undergo ~20% mass loss followed by approximately 5−6% mass loss attributed to the consecutive loss of the HI followed by the CH$_3$NH$_2$ components.[57]

$$CH_3NH_3PbI_3(s) \rightarrow CH_3NH_3I(aq) + PbI_2(s) \tag{11}$$

$$CH_3NH_3I(aq) \rightarrow CH_3NH_2(aq) + HI(aq) \tag{12}$$

The overall reaction can occur from the abovementioned equations

$$CH_3NH_3PbI_3(s) \rightarrow CH_3NH_3I(aq)$$
$$\rightarrow PbI_2(s) + CH_3NH_2(aq) + HI(aq) \tag{13}$$
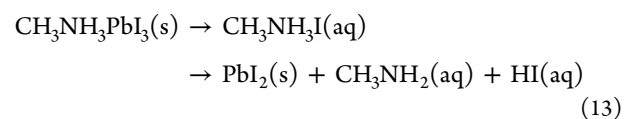
In highly humid conditions, the fast degradation of perovskite was observed which formed more superoxide radicals at grain boundaries. The elemental composition and the stoichiometry of the precursors are the main factors that control the structural stability and morphological properties of the perovskites.

From the TGA spectrum of $KMnO_4$-doped $MAPbI_3$, the fractions of weight loss due to the decomposition of water and KI from the $KMnO_4$ doping were observed in the temperature range of ~110−180 °C. Additionally, the PbI_2 weight loss of ~72.18% was observed in the temperature range of ~400−580 °C, with a slightly improved threshold of decomposition temperature (T_d) at ~568.33 °C. In continuation, MAI and DMF were calculated to be ~22.7 and ~10.4%, respectively, in the $MAI \cdot PbI_2 \cdot DMF$ intermediate complex. Hence, the overall thermal stability of the $KMnO_4$-doped perovskite (Figure 4b) was found to be enhanced at the threshold decomposition temperature (T_d = 568 °C), compared to the undoped perovskite (T_d = 555 °C), under ambient conditions. The high thermal stability of the $KMnO_4$-doped methylammonium lead halide perovskite makes it a good candidate for future applications. The remaining residues of $KMnO_4$-doped perovskite microrods may be various decomposition products and/or impurities. Differential scanning calorimetry (DSC) (Figure 4c) was also applied to detect the phase conversion and various transitions for the clear thermal behavior of the micrometer-long microrods. The reduction in glass transition temperature (T_g) from +51.26 to −20.55 °C was observed after doping of $KMnO_4$ in perovskite. Additionally, melting transition temperature (T_m) of the $KMnO_4$-doped perovskite also reduced compared to the undoped perovskite attributed to the phase conversion at low temperature during heating.[58]

XPS Analysis. To investigate various elemental bonding and structural confirmation, the $KMnO_4$-doped and -undoped perovskite materials were characterized by XPS analysis (Figure 5). Two symmetric and strong peaks were observed for the K $2p_{3/2}$ and K $2p_{1/2}$ states at a binding energy of 293.07 and 295.86 eV, respectively, because of potassium ion doping. The sharp K 2p peaks (Figure 5a) are related to the insertion of potassium cations in the perovskite crystal lattice. Additionally, XPS spectra with peak-fit processing for Mn $2p_{3/2}$ and Mn $2p_{1/2}$ in the doped perovskite exhibited an Mn $2p_{3/2}$ peak (Figure 5b) at a binding energy of 642.0 eV. However, three convoluted fitted peaks were found from the original peak with binding energies at 641.13, 644.59, and 653.18 eV, which might be attributed to the binding energy of Mn $2p_{3/2}$ in various oxidation states.[59] In the XPS spectrum of the undoped perovskite, the sharp and symmetric peaks of Pb $4f_{7/2}$ (binding energy at ~138.11 eV) and Pb $4f_{5/2}$ (binding energy at 143.00 eV) were attributed to the Pb^{2+} cations. The lead peaks displayed a spin−orbit splitting (ΔE) of ~4.89 eV with no trace of lead metallic peaks.

On the other hand, a slight reduction in the binding energy of both Pb^{2+} cation peaks (Pb $4f_{7/2}$ at ~137.92 eV and Pb $4f_{5/2}$ at ~142.78 eV) was observed after $KMnO_4$ doping of perovskite. Additionally, some amount of metallic lead peaks also appeared because of the formation of metal clusters in the doped perovskite.[49]

The spin−orbit splitting energy of $KMnO_4$-doped perovskite also decreased (ΔE = ~4.86 eV), confirming the insertion of $KMnO_4$ in the perovskite crystal lattice. The Pb $4f_{7/2}$ spectrum (Figure 5c) of $ITO/TiO_2/KMnO_4$-doped $MAPbI_3$ was composed of two convoluted peaks at ~137.92 and ~136.4

eV, which were assigned to $MAPbI_3$ and the Pb metal peak, respectively. In addition, the Pb $4f_{5/2}$ signal of the $ITO/TiO_2/MAPbI_3$ film displayed two convoluted peaks at ~142.78 eV for $MAPbI_3$ and at ~141.2 eV, which was attributed to the Pb metal with no traces of the PbO component. For the doped perovskite, the I 3d XPS spectrum (Figure 5d) showed two sharp and symmetric peaks for the iodine oxidation states. The I $3d_{5/2}$ peak (binding energy ~619.06 eV) for PbI_2 in the $ITO/TiO_2/KMnO_4$-doped perovskite film showed a spin−orbit splitting energy of ~11.49 eV with an I $3d_{3/2}$ (~630.4 eV) peak. From the I $3d_{5/2}$ plots, there was no trace of the I_2 peak around ~619.9 eV, unlike the strong ~618.91 eV peak for $MAPbI_3$. Recently, some authors have predicted that oxygen defects induced by the substitution of Pb or I in $CH_3NH_3PbI_3$ might produce new intraband states in the band gap that can attract an electron or hole.[60]

The XPS peaks at binding energy of ~285, ~400, and ~532 eV attributed to C 1s, N 1s, and O 1s element of the $KMnO_4$-doped perovskite microrods (Figure S4) which suggests the various bonding interactions. In the C 1s spectrum (Figure S4a), the five convoluted peaks were observed at the binding energy of ~283.78, ~284.75, ~285.71, ~286.81, and 288.23 eV. The XPS peak at ~283.78 eV belongs to the sp^2 C−C bond along with high intensity peaks at ~284.75 eV which is consistent to the sp^3 C−C bonds of methylamine and ~285.71 eV for the C−N bond of perovskite. Additionally, the low-intensity shoulder peaks at the binding energy of ~286.81 and ~288.23 eV were attributed to the C−O and C=O bonds, respectively, with high binding energy of the $KMnO_4$-doped perovskite microrods.[51] The O 1s spectra (Figure S4b) of the $KMnO_4$-doped perovskite microrods display two convoluted peaks of low intensity at ~530.08 and ~533.56 eV (for O=C−O) related to metal-oxide bond, metal−carbon bond, and associated to adsorbed OH^- and O_2^- ions. The high-intensity peak at a binding energy of ~531.72 eV is attributed to the C−O bonding for the doped perovskite microrods. From the N 1s XPS spectra (Figure S4c), the highest intensity peak observed at ~401.60 eV was for the sp^3 C−N bond peak of methylamine of perovskite. The low binding energy peak at ~399.89 eV is associated with nitrogen bonded to carbon (C−NH) and ~402.09 eV corresponding to $C−NH_3$ peak bonded to carbon, respectively. In continuation, the presence of weak hydrogen bonds in the protonated MA^+ ion ($CH_3NH_3^+$) is the main cause of decomposition of $MAPbI_3$. The C=O and C−O oxidation peaks are hard to distinguish because of the widening of the peaks and induce degradation of perovskite materials in the ambient atmosphere.[61]

Fourier-Transform Infrared Spectroscopy. In perovskite materials, IR spectroscopy (Figure S5) is used to investigate various bonding patterns and to locate the important functional groups. For perovskite, the N−H stretch vibrations around 3180 cm^{-1} were observed for both the perovskites. The strength of hydrogen bonding in MA salts ($N^+−H \cdots X$) has a great effect on the N−H stretch bands at room temperature. Therefore, as hydrogen bonding decreases, the N−H band positions for MAI salts increase as the electronegativity of the halide decreases (Cl > Br > I series). In perovskites, the N−H stretch bands have a contrary trend because of the increasing polarizability of the Pb−X bond.[53] Moreover, the N−H bands at ~3180 cm^{-1} (in the undoped perovskite) are related to the strong hydrogen bonding tendency in $KMnO_4$-doped perovskite (~3210 cm^{-1}), at stretching vibrations above ~3200 cm^{-1}.[62] The undoped
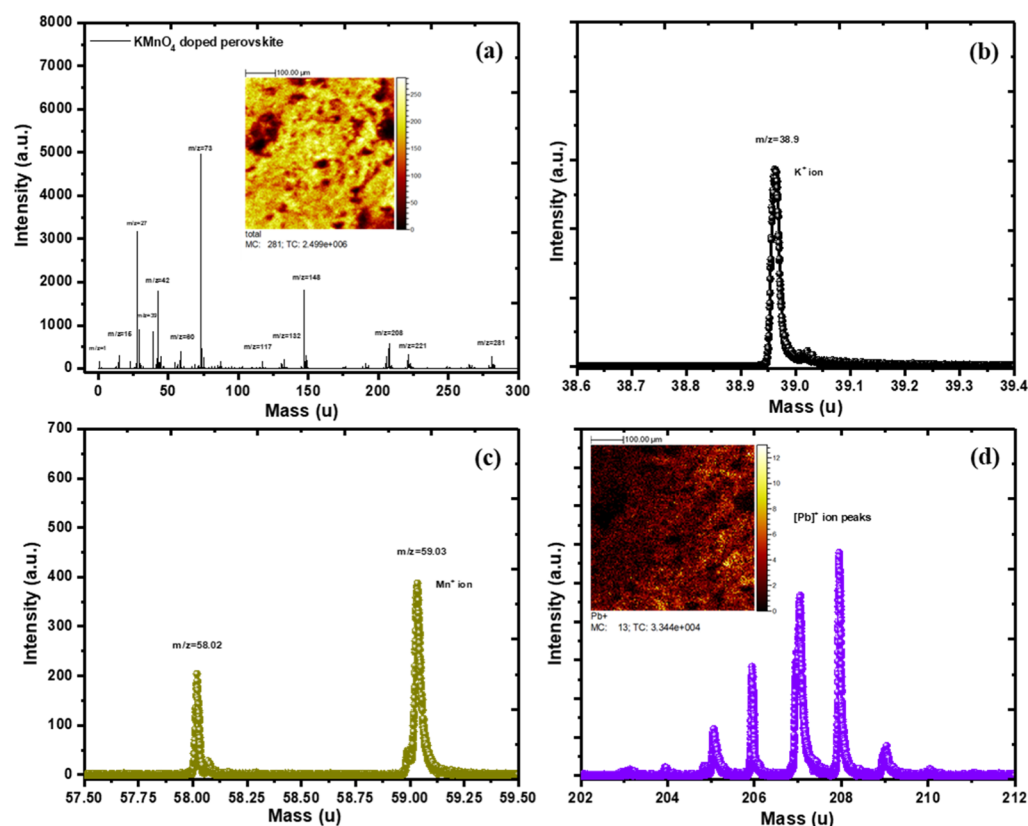
Figure 6. TOF-SIMS spectra of $KMnO_4$-doped perovskite (a) full spectrum with the inset image, (b) potassium cation peak, (c) manganese cation peaks, (d) lead cation peaks with the inset image.

perovskite displays some important vibration peaks of CH_3NH_3 at ~1641, ~1032, ~954 cm^{-1} for the C−H and N−H vibrations, NH_3^+ at ~1469 cm^{-1}, symmetrical CH_3−I at ~1385 cm^{-1} for C−H stretching, symmetric CH_3 peaks at ~1423 cm^{-1}, and so forth. After $KMnO_4$ doping, most of the characteristic peaks in the perovskite were reduced in the vibration positions, revealing that $KMnO_4$ had been successfully doped into the perovskite lattice. The IR spectra of perovskite powder (Figure S5a) exhibited powdered PbI_2· DMF and $MAI·PbI_2·DMF$ peaks at ~1020 cm^{-1} for $PbI_2·DMF$ which shifted to a lower wavenumber of ~1015 cm^{-1} for intermediates (Figure S5b) in the doped perovskite. Furthermore, the intensity of the higher wavenumber contribution of $MAPbI_3$ in the range of ~175−450 cm^{-1} is associated with MA torsional modes and lower wavenumber region (75−150 cm^{-1}) associated with the Pb−I−Pb cage for the libration modes of the MA$^+$ cation.[63]

Fourier-Transform Raman Spectroscopy. Raman spectroscopy measurements (Figure S5) were applied to locate the polarization disorder from MA$^+$ cations before and after doping of $KMnO_4$ in perovskite microrods and its effect on inorganic cage (PbI_6) distortion. The Raman spectra with Gaussian fit curves explore the deconvoluted peaks of perovskites, as shown in Figure S5c,d for undoped and $KMnO_4$-doped perovskite microrods, respectively. The three distinct regions of Raman spectra are named as internal vibrations of the MA cations (300−3200 cm^{-1}), libration/ translation and spinning of the organic (60−180 cm^{-1}) cations. Furthermore, the Raman peaks observed below 50 cm^{-1} correspond to internal vibrations of the inorganic PbI_3 network, whereas the peaks at ~116, ~121, and ~139 cm^{-1}
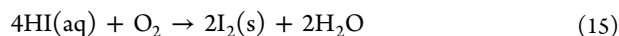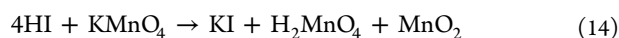
correspond to libration modes of the MA cations.[64] In plots, the characteristic peaks of the MA$^+$ cation with libration or translational peaks at ~167 cm^{-1} and torsional motion of ~206.16 cm^{-1} were observed for the perovskite microrods after $KMnO_4$ doping. After doping, a high intensity and enhanced energy band at ~121 cm^{-1} has been assigned to the coupled mode of the cage and MA$^+$ libration peaks compared to undoped perovskite at ~116.15 cm^{-1} with low intensity. Owing to the slight decrease in the crystallite grain size, the inorganic cage-assigned peak exhibits increased intensity, resulting in lower degree of the order lattice structure with enhanced coupling between the inorganic cage and MA$^+$ cations. The torsional motion of the MA$^+$ cation peak at 273.31 cm^{-1} undergoes high frequency toward ~293.43 cm^{-1} at room temperature, indicating the stiffening of the MA$^+$ cation vibrations of $KMnO_4$-doped perovskite microrods.[65]

Time-of-Flight Secondary-Ion Mass Spectrometry. TOF-SIMS is a highly sensitive technique capable of providing intrinsic information about inorganic and organic materials. Generally, TOF-SIMS data signals (Figure 6) are measured as a function of the mass-to-charge ratio (m/z) with charged secondary ion intensity as a mass spectrum; hence, it is an excellent way to verify the possible degradation products of powder perovskite materials. TOF-SIMS can furnish the distribution of various types of cations and anions in powder or thin films. In addition, Pb$^+$ is the main isotope of Pb metal which displayed a positive secondary-ion signal at 208 in the m/z spectrum, but a doubly charged secondary-ion (Pb^{2+}) signal can also be found at 104 on the m/z spectrum. In the undoped perovskite (Figure S6), the positive-ion high-intensity peaks were observed at m/z ratios of 1, 15, 18, 28, 32, 42, 73,

87, 127, 147, 208, 254, 461, and were attributed to H$^+$, [CH$_3$]$^+$, [NH$_4$]$^+$ or H$_2$O, [CH$_3$NH$_3$]$^+$, (CH$_3$)$_2$NCHO, I, (CH$_3$NH$_3$)$_4$N, [Pb]$^+$, and I$_2$. Some important peaks for the methyl ammonium ion and (tetramethyl ammonium) amine ion were also observed because of excess methyl ammonium ions and solvent interactions with the perovskite.[66] After degradation, some byproducts might create defects within the perovskite lattice via unstable intermediate states coordinated with solvents. The TOF-SIMS analysis (Figure 2) identified the peaks of [CH$_3$]$^+$, [CH$_3$NH$_3$]$^+$, [Pb]$^+$, and I$_2$, which correspond to the degradation mechanism of perovskites. The antibonding orbitals in the CH$_3$NH$_3^+$ cation form a metastable intermediate CH$_3$I−PbI$_2$ state defect because of lowering of the C−N bond strength and produced HI which reacts with atmospheric O$_2$ to produce I$_2$ in the solid-phase reactions

The HI obtained from eq 13 might interact with the dopant, atmospheric oxygen, and humidity as

$$4HI + KMnO_4 \rightarrow KI + H_2MnO_4 + MnO_2 \tag{14}$$

$$4HI(aq) + O_2 \rightarrow 2I_2(s) + 2H_2O \tag{15}$$

$$2HI(aq) \rightarrow H_2(g) + I_2 \tag{16}$$

In the KMnO$_4$ doped perovskite, the TOF-SIMS plots (Figure 6) showed clear peaks of the K$^+$ cation and Mn$^+$ cation, revealing the successful simultaneous induction of K$^+$ cations and Mn^{2+} cations in perovskite. During decomposition of the KMnO$_4$-doped perovskite microrods, lead metallic (Pb^0) clusters were formed using moisture as a catalyst, which converted the Pb^{2+} cation into metallic Pb (Pb^0) clusters. In the spectra, the observed peaks at m/z ratios of 1, 15, 29, 39, 42, 60, 73, 127, 148, 208, 254, and 461 were attributed to H$^+$, [CH$_3$]$^+$, K$^+$, [CH$_3$NH$_3$]$^+$, Mn$^+$, (CH$_3$)$_2$NCHO, I, (CH$_3$NH$_3$)$_4$N, and [Pb]$^+$ ions. The clear and sharp peaks at m/z 39 and m/z 59 were attributed to the inclusion of K$^+$ and Mn^{2+} ions in the perovskite. Owing to the hydrophilic nature, MAI reacts with oxygen and water in the environment, which lowers the stability of CH$_3$NH$_3$PbI$_3$ at room temperature.

Furthermore, when CH$_3$NH$_3$PbI$_3$ is exposed to a humid environment, monohydrated intermediate crystal phases are formed via reversible reactions at room temperature, which is converted to CH$_3$NH$_3$PbI$_3$ again after annealing. Generally, moisture-based degradation of perovskites starts at the grain boundaries in thin films, and increasing the perovskite grain size can enhance their stability in moisture because water molecules permeate more efficiently through the grain boundaries. In this manuscript, the precursor solutions are mixed in stoichiometric (1:1) ratios. During doping of the KMnO$_4$ solution at the precursor solution (CH$_3$NH$_3$I/PbI$_2$, 1:1) ratio, an in situ cation dissociation (CH$_3$NH$_3^+$) occurs during perovskite synthesis, and the excess iodide ions (I$^-$) form some potassium iodide, iodoplumbate complexes such as PbI$_3^-$ and PbI$_4^{2-}$, and so forth. The energy released by the crystal formation reaction might further dissociate the free CH$_3$NH$_3$I molecules and iodoplumbate complexes into smaller and more stable molecules such as CH$_3$I and NH$_3$. The slight excess of PbI$_2$ can improve the morphology by increasing the grain size, uniformity, and passivating defects at grain boundaries.[67,68]

CONCLUSIONS

In this work, thermally stable KMnO$_4$-doped methylammonium lead iodide, CH$_3$NH$_3$PbI$_3$ perovskite microrods were

developed via the antisolvent crystallization method. KMnO$_4$ was efficiently doped into a CH$_3$NH$_3$PbI$_3$ perovskite lattice structure via a solution-based one-step method and improved its electrical, optical, and thermal properties. The XRD spectra of the microrods revealed an intermolecular d-spacing of ∼0.22 nm with a crystallite size of ∼41 nm. During the synthesis of the KMnO$_4$-doped perovskite microrods, a low boiling-point solvent, anhydrous chloroform, was employed as an antisolvent to facilitate and control the growth of KMnO$_4$-doped perovskite microrods. The as-synthesized KMnO$_4$-doped perovskite microrods retained the pristine perovskite crystalline phases and lowered the energy band gap (∼1.57 eV) using the Tauc plots because of improved light absorption and narrow fluorescence emission bands (fwhm < 10 nm) after doping. Additionally, the lowering of the Urbach energy was observed after doping in perovskite. Furthermore, W−H plots were applied to calculate the structural modifications as the lattice strain (∼4.42 × 10^{-5}), Goldsmith tolerance factor (∼0.89), and high dislocation density (∼5.82 × 10^{-4}) of the KMnO$_4$-doped perovskite microrods.

EXPERIMENTAL SECTION

Materials and Methods. During the experiment, all the reagents and chemicals were used as received without any further purification. Lead(II) iodide (PbI$_2$) and MAI were purchased from Sigma-Aldrich and TCI Chemicals (Japan), respectively. DMF (anhydrous, 99.8%) and isopropanol (IPA) were supplied by Sigma-Aldrich.

Characterizations. To analyze the structural properties of the samples, HR XRD spectra were obtained in the range of 5−80° with Cu Kα radiation (λ = 1.5406 Å) using an X-ray diffractometer (Empyrean, Panalytical, USA). The absorption spectra were calibrated against the pure glass substrates. UV−visible spectra of perovskite films were analyzed using a Cary 5000 UV−vis−NIR spectrophotometer (Agilent Technologies) with D$_2$ and tungsten lamps in the range of 300−1100 nm wavelength. Fluorescence spectra of the undoped and doped perovskite were collected using a PerkinElmer/LS 55 Fluorescence Spectrometer at the excitation wavelength of 500 nm. UHR-FESEM images were collected from the Hitachi (SU 8230) instrument for the fine powder of undoped and doped perovskite with their elemental mapping images. Fourier-transform infrared (FT-IR) spectroscopy (Nicolet Continuum, Thermo Fisher Scientific, USA) was performed in the attenuated total reflectance mode at a resolution of 4 cm^{-1}. FT-IR spectra were collected in the range of 4000−650 cm^{-1} at the room temperature. Raman spectroscopy was performed using a confocal Raman spectrometer (Thermo Fisher Scientific, Nicolet Almeca XRA) with a λ_{ex} of 532 nm at room temperature. TGA measurements were performed in the temperature range of 25−600 °C in air (flow rate of 40 mL/min) using a TGA (Auto Q500, TA Instruments-Waters Korea) for thermal stability of undoped and doped perovskite microrods. The phase conversion of the sample was analyzed by DSC (Discovery DSC, TA Instruments) with temperature. The elemental composition was measured using XPS analysis in an ultrahigh vacuum setup equipped with a monochromatic Al Kα X-ray source (1486.6 eV) (Escalab 250Xi, Thermo Fisher Scientific, USA) for undoped and doped perovskite microrods. In the XPS data, the fitted peaks were treated with background corrections and found various corresponding convoluted peaks using Gaussian fit curves. HR-TEM (S-4800, Hitachi, Japan) was employed to examine the crystal

images and patterns of the undoped and doped perovskite microrods. ToF-SIMS was applied to determine the elemental mass compositions of undoped and doped perovskite microrods. ToF-SIMS is capable of detecting ions over a large mass range of 1−10,000 units. For negatively and positively charged secondary ions, the ToF-SIMS analysis was carried out with a TOF-SIMS 5−100 system from ION-TOF GmbH (Münster, Germany) using a maximum beam energy of the 30 keV Bi^{3+} cluster ion beam guns.

Synthesis of Methyl Ammonium Iodide. In a typical experimental procedure, an equimolar amount of hydroiodic acid (15 mL, 57 wt % in water, Sigma-Aldrich) was added dropwise to an aqueous solution of methylamine (13.5 mL, 40 wt % in water, Sigma-Aldrich) in an ice bath with stirring. The ice-cold solution was stirred for 2 h, and the solvent was evaporated. The white-colored product was dissolved in ethanol and recrystallized using diethyl ether. The obtained shining white shining crystals were washed three times using diethyl ether and dried in vacuum for 24 h.

Synthesis of Undoped $MAPbI_3$ Microrods. The undoped perovskite microrods were synthesized by mixing the equimolar solutions of PbI_2 and MAI (1:1 ratio) in DMF and stirred at 100 °C for 24 h to obtain a yellow perovskite solution. Thus, the obtained doped perovskite solution (PbI_2/MAI, 1:1 ratio, 50 μL) was added dropwise in anhydrous chloroform (5 mL) to achieve micrometer-long (<10 μm) and diameter of few micrometer (<3 μm) rods as black powder at room temperature. The thus-obtained undoped perovskite microrods were further annealed at 100 °C for 6 h to finally develop stable undoped perovskite microrods as dark black powder.

Synthesis of $KMnO_4$-Doped $MAPbI_3$ Microrods. For the $KMnO_4$-doped perovskite microrods synthesis, the equimolar solutions of PbI_2 and MAI were prepared (1:1 ratio) in DMF and stirred at 100 °C for 24 h to obtain the yellow solution of perovskite. Freshly prepared $KMnO_4$ (5 mg/mL, DMF) solution was added dropwise and stirred for 12 h at 100 °C, resulting in a red-brown-colored solution. Thus-obtained doped perovskite solution (PbI_2/MAI, 1:1 ratio, 50 μL) was added dropwise in stirred anhydrous chloroform (5 mL) to develop $KMnO_4$-doped perovskite microrods as black powder at room temperature. The as-obtained $KMnO_4$-doped perovskite microrods were further washed several times using chloroform and annealed at 100 °C for evaporation of the excess solvent. Finally, doped perovskite microrods were further annealed at 100 °C for 6 h to obtain thermally stable $KMnO_4$ perovskite microrods as dark black powder.

Fabrication Procedure of Undoped and $KMnO_4$-Doped $MAPbI_3$ Thin Films. For fabrication, the ITO glass was cleaned in a sequence with a detergent and deionized water, acetone, and IPA via sonication for 10 min for each at room temperature. A thin TiO_2 compact layer was deposited on a cleaned ITO substrate by spin-coating using a solution composed of 0.15 M titanium diisopropoxide bis-(acetylacetonate) (75 wt % in 2-propanol, Sigma-Aldrich) in 2-propanol (99.9% Sigma-Aldrich) at 4000 rpm for 30 s. The coated ITO substrate was then dried at 120 °C for 5 min, followed by calcination at 450 °C for 30 min. Furthermore, TiO_2 paste (Titania Paste, Dyesol) diluted in ethanol (5 mg/mL) was spin-coated on the compact TiO_2-coated ITO substrate at 6000 rpm for 30 s to get a mesoporous TiO_2 film at ambient temperature. After coating, the bilayer samples were dried at 120 °C for 5 min and then sintered at 450 °C for 30

min. On the deposited TiO_2 layer, thin films of undoped and $KMnO_4$-doped $MAPbI_3$ perovskite solutions in anhydrous DMF were deposited by one-step solution spin-casting of the PbI_2/MAI (1:1, ratio) mixture in anhydrous DMF at 4000 rpm for 40 s in an ambient atmosphere. Thus, the obtained films were annealed at 100 °C for 10 min in ambient air to obtain dark-brown-colored perovskite films.

■ ASSOCIATED CONTENT

ⓢ Supporting Information

The Supporting Information is available free of charge at https://pubs.acs.org/doi/10.1021/acsomega.0c01667.

XRD spectra, UHR-FESEM images, UV−vis spectra with Tauc plots, fluorescence spectra with Gaussian fit, XPS analysis, and FT-IR, and TOF-SIMS spectrometry of undoped perovskite microrods (PDF)

■ AUTHOR INFORMATION

Corresponding Author

Jae Hyun Kim − *Division of Energy Technology, Daegu Gyeongbuk Institute of Science & Technology (DGIST), Daegu 42988, Republic of Korea;* ⓞ orcid.org/0000-0003-2824-0113; Email: jaehyun@dgist.ac.kr

Author

Mohammed Nazim − *Division of Energy Technology, Daegu Gyeongbuk Institute of Science & Technology (DGIST), Daegu 42988, Republic of Korea*

Complete contact information is available at:
https://pubs.acs.org/10.1021/acsomega.0c01667

Notes

The authors declare no competing financial interest.

■ ACKNOWLEDGMENTS

■ REFERENCES

(1) Ball, J. M.; Lee, M. M.; Hey, A.; Snaith, H. J. Low-temperature processed meso-superstructured to thin-film perovskite solar cells. *Energy Environ. Sci.* **2013**, *6*, 1739−1743.

(2) Chang, C.-Y.; Chu, C.-Y.; Huang, Y.-C.; Huang, C.-W.; Chang, S.-Y.; Chen, C.-A.; Chao, C.-Y.; Su, W.-F. Tuning perovskite morphology by polymer additive for high efficiency solar cell. *ACS Appl. Mater. Interfaces* **2015**, *7*, 4955−4961.

(3) Chueh, C.-C.; Liao, C.-Y.; Zuo, F.; Williams, S. T.; Liang, P.-W.; Jen, A. K.-Y. The roles of alkyl halide additives in enhancing perovskite solar cell performance. *J. Mater. Chem. A* **2015**, *3*, 9058−9062.

(4) Brenner, T. M.; Egger, D. A.; Kronik, L.; Hodes, G.; Cahen, D. Hybrid organic-inorganic perovskites: low-cost semiconductors with intriguing charge-transport properties. *Nat. Rev. Mater.* **2016**, *1*, 15007.

(5) Li, C.; Wang, A.; Xie, L.; Deng, X.; Liao, K.; Yang, J.-a.; Li, T.; Hao, F. Emerging alkali metal ion (Li^+, Na^+, K^+ and Rb^+) doped perovskite films for efficient solar cells: recent advances and prospects. *J. Mater. Chem. A* **2019**, *7*, 24150−24163.

(6) Zhao, W.; Yao, Z.; Yu, F.; Yang, D.; Liu, S. F. Alkali metal doping for improved $CH_3NH_3PbI_3$ perovskite solar Cells. *Adv. Sci.* **2018**, *5*, 1700131.

(7) Xiao, M.; Huang, F.; Huang, W.; Dkhissi, Y.; Zhu, Y.; Etheridge, J.; Gray-Weale, A.; Bach, U.; Cheng, Y.-B.; Spiccia, L. A fast deposition-crystallization procedure for highly efficient lead iodide perovskite thin-film solar cells. *Angew. Chem., Int. Ed.* **2014**, *53*, 9898−9903.

(8) Wu, K.; Liang, G.; Shang, Q.; Ren, Y.; Kong, D.; Lian, T. Ultrafast interfacial electron and hole transfer from $CsPbBr_3$ perovskite quantum dots. *J. Am. Chem. Soc.* **2015**, *137*, 12792−12795.

(9) Braly, I. L.; deQuilettes, D. W.; Pazos-Outón, L. M.; Burke, S.; Ziffer, M. E.; Ginger, D. S.; Hillhouse, H. W. Hybrid perovskite films approaching the radiative limit with over 90% photoluminescence quantum efficiency. *Nat. Photonics* **2018**, *12*, 355−361.

(10) Yakunin, S.; Sytnyk, M.; Kriegner, D.; Shrestha, S.; Richter, M.; Matt, G. J.; Azimi, H.; Brabec, C. J.; Stangl, J.; Kovalenko, M. V.; Heiss, W. Detection of X-ray photons by solution-processed organic-inorganic perovskites. *Nat. Photonics* **2015**, *9*, 444−449.

(11) Mao, W.; Zheng, J.; Zhang, Y.; Chesman, A. S. R.; Ou, Q.; Hicks, J.; Li, F.; Wang, Z.; Graystone, B.; Bell, T. D. M.; Rothmann, M. U.; Duffy, N. W.; Spiccia, L.; Cheng, Y.-B.; Bao, Q.; Bach, U. Controlled growth of monocrystalline organo-lead halide perovskite and its application in photonic devices. *Angew. Chem., Int. Ed.* **2017**, *56*, 12486−12491.

(12) Lee, M. M.; Teuscher, J.; Miyasaka, T.; Murakami, T. N.; Snaith, H. J. Efficient Hybrid Solar Cells Based on Meso-Super-structured Organometal Halide Perovskites. *Science* **2012**, *338*, 643−647.

(13) Kim, H.-S.; Lee, J.-W.; Yantara, N.; Boix, P. P.; Kulkarni, S. A.; Mhaisalkar, S.; Grätzel, M.; Park, N.-G. High efficiency solid-state sensitized solar cell-based on submicrometer rutile TiO_2 microrod and $CH_3NH_3PbI_3$ perovskite sensitizer. *Nano Lett.* **2013**, *13*, 2412−2417.

(14) Liu, M.; Johnston, M. B.; Snaith, H. J. Efficient planar heterojunction perovskite solar cells by vapour deposition. *Nature* **2013**, *501*, 395−398.

(15) Gaspera, E. D.; Peng, Y.; Hou, Q.; Spiccia, L.; Bach, U.; Jasieniak, J. J.; Cheng, Y.-B. Ultra-thin high efficiency semitransparent perovskite solar cells. *Nano Energy* **2015**, *13*, 249−257.

(16) Protesescu, L.; Yakunin, S.; Bodnarchuk, M. I.; Krieg, F.; Caputo, R.; Hendon, C. H.; Yang, R. X.; Walsh, A.; Kovalenko, M. V. Nanocrystals of cesium lead halide perovskites ($CsPbX_3$, X = Cl, Br, and I): Novel optoelectronic materials showing bright emission with wide color gamut. *Nano Lett.* **2015**, *15*, 3692−3696.

(17) Liang, J.; Liu, Z.; Qiu, L.; Hawash, Z.; Meng, L.; Wu, Z.; Jiang, Y.; Ono, L. K.; Qi, Y. Enhancing optical, electronic, crystalline, and morphological properties of cesium lead halide by Mn substitution for high-stability all-inorganic perovskite solar cells with carbon electrodes. *Adv. Energy Mater.* **2018**, *8*, 1800504.

(18) Yakunin, S.; Protesescu, L.; Krieg, F.; Bodnarchuk, M. I.; Nedelcu, G.; Humer, M.; De Luca, G.; Fiebig, M.; Heiss, W.; Kovalenko, M. V. Low-threshold amplified spontaneous emission and lasing from colloidal nanocrystals of caesium lead halide perovskites. *Nat. Commun.* **2015**, *6*, 8056.

(19) Tan, Z.-K.; Moghaddam, R. S.; Lai, M. L.; Docampo, P.; Higler, R.; Deschler, F.; Price, M.; Sadhanala, A.; Pazos, L. M.; Credgington, D.; Hanusch, F.; Bein, T.; Snaith, H. J.; Friend, R. H. Bright light-emitting diodes based on organometal halide perovskite. *Nat. Nanotechnol.* **2014**, *9*, 687.

(20) He, T.; Li, J.; Ren, C.; Xiao, S.; Li, Y.; Chen, R.; Lin, X. Strong two-photon absorption of Mn-doped $CsPbCl_3$ perovskite nanocrystals. *Appl. Phys. Lett.* **2017**, *111*, 211105.

(21) Zhou, H.; Chen, Q.; Li, G.; Luo, S.; Song, T.-b.; Duan, H.-S.; Hong, Z.; You, J.; Liu, Y.; Yang, Y. Interface engineering of highly efficient perovskite solar cells. *Science* **2014**, *345*, 542−546.

(22) Jaramillo-Quintero, O. A.; Sanchez, R. S.; Rincon, M.; Mora-Sero, I. Bright visible-infrared light emitting diodes based on hybrid

halide perovskite with Spiro-OMeTAD as a hole-injecting layer. *J. Phys. Chem. Lett.* **2015**, *6*, 1883−1890.

(23) Parobek, D.; Dong, Y.; Qiao, T.; Son, D. H. Direct hot-injection synthesis of Mn-doped $CsPbBr_3$ nanocrystals. *Chem. Mater.* **2018**, *30*, 2939−2944.

(24) Náfrádi, B.; Szirmai, P.; Spina, M.; Lee, H.; Yazyev, O. V.; Arakcheeva, A.; Chernyshov, D.; Gibert, M.; Forró, L.; Horváth, E. Optically switched magnetism in photovoltaic perovskite CH3NH3-(Mn:Pb)I3. *Nat. Commun.* **2016**, *7*, 13406.

(25) Guria, A. K.; Dutta, S. K.; Adhikari, S. D.; Pradhan, N. Doping Mn^{2+} in lead halide perovskite nanocrystals: Successes and challenges. *ACS Energy Lett.* **2017**, *2*, 1014−1021.

(26) Klug, M. T.; Osherov, A.; Haghighirad, A. A.; Stranks, S. D.; Brown, P. R.; Bai, S.; Wang, J. T.-W.; Dang, X.; Bulović, V.; Snaith, H. J.; Belcher, A. M. Tailoring metal halide perovskites through metal substitution: Influence on photovoltaic and material properties. *Energy Environ. Sci.* **2017**, *10*, 236−246.

(27) Mir, W. J.; Jagadeeswararao, M.; Das, S.; Nag, A. Colloidal Mn-doped cesium lead halide perovskite nanoplatelets. *ACS Energy Lett.* **2017**, *2*, 537−543.

(28) Liu, W.; Lin, Q.; Li, H.; Wu, K.; Robel, I.; Pietryga, J. M.; Klimov, V. I. Mn^{2+}-doped lead halide perovskite nanocrystals with dual-color emission controlled by halide content. *J. Am. Chem. Soc.* **2016**, *138*, 14954−14961.

(29) Zhao, P.; Yin, W.; Kim, M.; Han, M.; Song, Y. J.; Ahn, T. K.; Jung, H. S. Improved carriers injection capacity in perovskite solar cells by introducing A-site interstitial defects. *J. Mater. Chem. A* **2017**, *5*, 7905−7911.

(30) Nam, J. K.; Chai, S. U.; Cha, W.; Choi, Y. J.; Kim, W.; Jung, M. S.; Kwon, J.; Kim, D.; Park, J. H. Potassium incorporation for enhanced performance and stability of fully inorganic cesium lead halide perovskite solar cells. *Nano Lett.* **2017**, *17*, 2028−2033.

(31) Jacobsson, T. J.; Svanström, S.; Andrei, V.; Rivett, J. P. H.; Kornienko, N.; Philippe, B.; Cappel, U. B.; Rensmo, H.; Deschler, F.; Boschloo, G. Extending the Compositional Space of Mixed Lead Halide Perovskites by Cs, Rb, K, and Na Doping. *J. Phys. Chem. C* **2018**, *122*, 13548−13557.

(32) Zhao, W.; Yao, Z.; Yu, F.; Yang, D.; Liu, S. F. Alkali metal doping for improved $CH_3NH_3PbI_3$ perovskite solar Cells. *Adv. Sci.* **2018**, *5*, 1700131−1700138.

(33) Jia, X.; Hu, Z.; Zhu, Y.; Weng, T.; Wang, J.; Zhang, J.; Zhu, Y. Facile synthesis of organic−inorganic hybrid perovskite $CH_3NH_3PbI_3$ microcrystals. *J. Alloys Compd.* **2017**, *725*, 270−274.

(34) Stoumpos, C. C.; Kanatzidis, M. G. Semiconducting tin and lead iodide perovskites with organic cations: Phase transitions, high mobilities, and near-infrared photoluminescent properties. *Inorg. Chem.* **2013**, *52*, 9019−9038.

(35) Ou, Q.; Bao, X.; Zhang, Y.; Shao, H.; Xing, G.; Li, X.; Shao, L.; Bao, Q. Band structure engineering in metal halide perovskite nanostructures for optoelectronic applications. *Nano Mater. Sci.* **2019**, *1*, 268−287.

(36) Yang, Z.; Cai, B.; Zhou, B.; Yao, T.; Yu, W.; Liu, S.; Zhang, W.-H.; Li, C. An up-scalable approach to $CH_3NH_3PbI_3$ compact films for high-performance perovskite solar cells. *Nano Energy* **2015**, *15*, 670−678.

(37) Palazon, F.; Akkerman, Q. A.; Prato, M.; Manna, L. X-ray lithography on perovskite nanocrystals films: From patterning with anion-exchange reactions to enhanced stability in air and water. *ACS Nano* **2016**, *10*, 1224−1230.

(38) Lin, C. C.; Meijerink, A.; Liu, R.-S. Critical red components for next-generation white LEDs. *J. Phys. Chem. Lett.* **2016**, *7*, 495−503.

(39) Saliba, M.; Matsui, T.; Seo, J.-Y.; Domanski, K.; Correa-Baena, J.-P.; Nazeeruddin, M. K.; Zakeeruddin, S. M.; Tress, W.; Abate, A.; Hagfeldt, A.; Grätzel, M. Cesium-containing triple cation perovskite solar cells: improved stability, reproducibility and high efficiency. *Energy Environ. Sci.* **2016**, *9*, 1989−1997.

(40) Lovrinčić, R.; Pucci, A. Infrared optical properties of chromium nanoscale films with a phase transition. *Phys. Rev. B: Condens. Matter Mater. Phys.* **2009**, *80*, 205404.

(41) Bartesaghi, D.; Ray, A.; Jiang, J.; Bouwer, R. K. M.; Tao, S.; Savenije, T. J. Partially replacing Pb^{2+} by Mn^{2+} in hybrid metal halide perovskites: Structural and electronic properties. *APL Mater.* **2018**, *6*, 121106.

(42) Levine, I.; Vera, O. G.; Kulbak, M.; Ceratti, D.-R.; Rehermann, C.; Márquez, J. A.; Levcenko, S.; Unold, T.; Hodes, G.; Balberg, I.; Cahen, D.; Dittrich, T. Deep defect states in wide-band-gap ABX_3 halide perovskites. *ACS Energy Lett.* **2019**, *4*, 1150−1157.

(43) Li, Z.; Yang, M.; Park, J.-S.; Wei, S.-H.; Berry, J. J.; Zhu, K. Stabilizing Perovskite Structures by Tuning Tolerance Factor: Formation of Formamidinium and Cesium Lead Iodide Solid-State Alloys. *Chem. Mater.* **2016**, *28*, 284−292.

(44) De Roo, J.; Ibáñez, M.; Geiregat, P.; Nedelcu, G.; Walravens, W.; Maes, J.; Martins, J. C.; Van Driessche, I.; Kovalenko, M. V.; Hens, Z. Highly dynamic ligand binding and light absorption coefficient of cesium lead bromide perovskite nanocrystals. *ACS Nano* **2016**, *10*, 2071.

(45) Luo, Y.; Khoram, P.; Brittman, S.; Zhu, Z.; Lai, B.; Ong, S. P.; Garnett, E. C.; Fenning, D. P. Direct observation of halide migration and its effect on the photoluminescence of methylammonium lead bromide perovskite single crystals. *Adv. Mater.* **2017**, *29*, 1703451.

(46) Wu, Y.; Wei, C.; Li, X.; Li, Y.; Qiu, S.; Shen, W.; Cai, B.; Sun, Z.; Yang, D.; Deng, Z.; Zeng, H. In situ passivation of $[PbBr_6]^{4-}$ octahedra toward blue luminescent $CsPbBr_3$ nanoplatelets with near 100% absolute quantum yield. *ACS Energy Lett.* **2018**, *3*, 2030−2037.

(47) Shi, Z.; Guo, J.; Chen, Y.; Li, Q.; Pan, Y.; Zhang, H.; Xia, Y.; Huang, W. Lead-free organic-inorganic hybrid perovskites for photovoltaic applications: recent advances and perspectives. *Adv. Mater.* **2017**, *29*, 1605005.

(48) Wang, Z.-K.; Li, M.; Yang, Y.-G.; Hu, Y.; Ma, H.; Gao, X.-Y.; Liao, L.-S. High efficiency Pb-in binary metal perovskite solar cells. *Adv. Mater.* **2016**, *28*, 6695.

(49) Zhou, Y.; Chen, J.; Bakr, O. M.; Sun, H.-T. Metal-doped lead halide perovskites: synthesis, properties, and optoelectronic applications. *Chem. Mater.* **2018**, *30*, 6589.

(50) Pan, A.; He, B.; Fan, X.; Liu, Z.; Urban, J. J.; Alivisatos, A. P.; He, L.; Liu, Y. Insight into the ligand-mediated synthesis of colloidal $CsPbBr_3$ perovskite nanocrystals: The role of organic acid, base, and cesium precursors. *ACS Nano* **2016**, *10*, 7943−7954.

(51) Baikie, T.; Fang, Y.; Kadro, J. M.; Schreyer, M.; Wei, F.; Mhaisalkar, S. G.; Graetzel, M.; White, T. J. Synthesis and crystal chemistry of the hybrid perovskite $CH_3NH_3PbI_3$ for solid-state sensitised solar cell applications. *J. Mater. Chem. A* **2013**, *1*, 5628−5641.

(52) Wang, J. T.-W.; Wang, Z.; Pathak, S.; Zhang, W.; deQuilettes, D. W.; Wisnivesky-Rocca-Rivarola, F.; Huang, J.; Nayak, P. K.; Patel, J. B.; Mohd Yusof, H. A.; Vaynzof, Y.; Zhu, R.; Ramirez, I.; Zhang, J.; Ducati, C.; Grovenor, C.; Johnston, M. B.; Ginger, D. S.; Nicholas, R. J.; Snaith, H. J. Efficient perovskite solar cells by metal ion doping. *Energy Environ. Sci.* **2016**, *9*, 2892−2901.

(53) Naphade, R.; Nagane, S.; Shanker, G. S.; Fernandes, R.; Kothari, D.; Zhou, Y.; Padture, N. P.; Ogale, S. Hybrid perovskite quantum nanostructures synthesized by electrospray antisolvent−solvent extraction and intercalation. *ACS Appl. Mater. Interfaces* **2016**, *8*, 854−861.

(54) Sun, Q.; Wang, S.; Zhao, C.; Leng, J.; Tian, W.; Jin, S. Excitation-dependent emission color tuning from an individual Mn-doped perovskite microcrystal. *J. Am. Chem. Soc.* **2019**, *141*, 20089−20096.

(55) Akshay, V. R.; Arun, B.; Mandal, G.; Vasundhara, M. Visible range optical absorption, Urbach energy estimation and paramagnetic response in Cr-doped TiO_2 nanocrystals derived by a sol−gel method. *Phys. Chem. Chem. Phys.* **2019**, *21*, 12991−13004.

(56) Choudhury, B.; Choudhury, A. Oxygen defect dependent variation of band gap, Urbach energy and luminescence property of anatase, anatase−rutile mixed phase and of rutile phases of TiO_2 nanoparticles. *Phys. E* **2014**, *56*, 364.

(57) Ahmad, Z.; Najeeb, M. A.; Shakoor, R. A.; Alashraf, A.; Al-Muhtaseb, S. A.; Soliman, A.; Nazeeruddin, M. K. Instability in $CH_3NH_3PbI_3$ perovskite solar cells due to elemental migration and chemical composition changes. *Sci. Rep.* **2017**, *7*, 15406.

(58) Olthof, S.; Meerholz, K. Substrate-dependent electronic structure and film formation of MAPbI3 perovskites. *Sci. Rep.* **2017**, *7*, 40267.

(59) Li, Y.; Zhao, Z.; Lin, F.; Cao, X.; Cui, X.; Wei, J. In situ observation of crystallization of methylammonium lead iodide perovskite from micro droplets. *Small* **2017**, *13*, 1604125.

(60) Kim, G.-H.; Jeong, J.; Jang, H.; Kim, J. W.; Kim, J. Y. Fast vaporizing anti-solvent for high crystalline perovskite to achieve high performance perovskite solar cells. *Thin Solid Films* **2018**, *661*, 122−127.

(61) Choi, Y. C.; Lee, S. W.; Kim, D.-H. Antisolvent-assisted powder engineering for controlled growth of hybrid $CH_3NH_3PbI_3$ perovskite thin films. *APL Mater.* **2017**, *5*, 026101.

(62) Yin, W.-J.; Shi, T.; Yan, Y. Unusual defect physics in $CH_3NH_3PbI_3$ perovskite solar cell absorber. *Appl. Phys. Lett.* **2014**, *104*, 063903.

(63) Lee, J.-W.; Kim, H.-S.; Park, N.-G. Lewis acid−base adduct approach for high efficiency perovskite solar cells. *Acc. Chem. Res.* **2016**, *49*, 311−319.

(64) Chen, Q.; Zhou, H.; Hong, Z.; Luo, S.; Duan, H.-S.; Wang, H.-H.; Liu, Y.; Li, G.; Yang, Y. Planar heterojunction perovskite solar cells via vapor-assisted solution process. *J. Am. Chem. Soc.* **2014**, *136*, 622−625.

(65) Boles, M. A.; Ling, D.; Hyeon, T.; Talapin, D. V. The surface science of nanocrystals. *Nat. Mater.* **2016**, *15*, 141−153.

(66) Jia, X.; Hu, Z.; Zhu, Y.; Weng, T.; Wang, J.; Zhang, J.; Zhu, Y. Facile synthesis of organic−inorganic hybrid perovskite $CH_3NH_3PbI_3$ microcrystals. *J. Alloys Compd.* **2017**, *725*, 270−274.

(67) Zhao, Y.; Zhu, K. CH_3NH_3Cl-assisted one-step solution growth of $CH_3NH_3PbI_3$: structure, charge-carrier dynamics, and photovoltaic properties of perovskite solar cells. *J. Phys. Chem. C* **2014**, *118*, 9412−9418.

(68) Li, Y.; Wang, J.; Yuan, Y.; Dong, X.; Wang, P. Anti-solvent dependent device performance in $CH_3NH_3PbI_3$ solar cells: the role of intermediate phase content in the as-prepared thin films. *Sustainable Energy Fuels* **2017**, *1*, 1041−1048.